1997 HST Calibration Workshop
Space Telescope Science Institute, 1997
S. Casertano, et al., eds.

The On-Orbit Optical Performance of STIS[1,2]

Charles W. Bowers[3]
Laboratory for Astronomy and Solar Physics, Goddard Space Flight Center, Greenbelt, MD 20771

Abstract. The Space Telescope Imaging Spectrograph (STIS) is a versatile, general purpose instrument installed aboard the *Hubble Space Telescope* in February, 1997. During the following Servicing Mission Orbital Verification (SMOV) period, STIS has been made operational and aligned, and initial checkout and calibration completed. The overall optical performance goals have largely been achieved and a summary of these results is presented.

1. Introduction

The Space Telescope Imaging Spectrograph (STIS) is a general purpose spectrograph installed aboard the Hubble Space Telescope in February, 1997. Through a number of optical modes, spatially resolved spectroscopy is possible from the ultraviolet to near infrared (115–1000nm) over fields of 25 and 50 arcseconds in the ultraviolet and visible respectively. Spectral resolving powers of 500-1000 may be achieved throughout the wavelength range in low resolution modes, and 10,000–20,000 in medium resolution modes. In the ultraviolet (115–310nm) medium and high resolution echelle spectroscopy may be obtained at resolutions of 30,000–45,000 and about 100,000. Custom manufactured gratings were acquired, tested, and installed to perform these functions (Content et al. 1997). Formats have been designed to provide simultaneous acquisition of spectra over wide bandpasses whenever possible to increase observing efficiency. A wide variety of slits and apertures are available to permit selection of many combinations of resolution and field in all modes. Camera modes are also available throughout the full instrument bandpass for target acquisition and for scientific imagery either in an unfiltered mode or using the small complement of available filters. Photon counting (MAMA) detectors are utilized in the ultraviolet with neutral density filters available to extend their capability for ultraviolet observations of brighter targets. A single CCD is provided for observations longward of 310nm.

Light entering STIS is corrected for the HST spherical aberration and astigmatism at the STIS field point by a two-element corrector system, analogous to the corrector pairs deployed by COSTAR. Following correction, a well focused image is formed at the STIS slit plane at which an appropriate slit, aperture or filter may be inserted in the light path using the slit wheel. Following the slit plane, light passes to an ellipsoidal collimator which redirects the beam toward an element on the mode select mechanism (MSM). Any one of

---

[1]The results reported here represent the efforts of many people, including the STIS Investigation Definition Team and personnel of the Goddard Space Flight Center, Ball Aerospace, and the Space Telescope Science Institute.

[2]Based on observations with the NASA/ESA *Hubble Space Telescope*, obtained at the Space Telescope Science Institute, which is operated by the Association of Universities for Research in Astronomy, Inc. (AURA), under NASA contract NAS5-26555.

[3]Co-investigator, STIS Investigation Definition Team

21 optics mounted on the MSM may be rotated into the collimated beam. The MSM can also tip or tilt the element as necessary for modes which must be scanned to cover the complete bandpass. All first order gratings, echelle cross dispersers and ultraviolet camera mirrors are located on the MSM, as well as several backup mode and transfer optics. Order sorters are mounted as appropriate in front of the MSM gratings. Selection of the particular element of the MSM results in light going toward one of the three detectors, either directly or via an echelle or fold mirror.

Further details of the STIS design and operations may be obtained from Woodgate et al. (1992, 1998) and the STScI *STIS Instrument Handbook* (Baum et al. 1996). The optical performance of STIS in a number of key areas is briefly summarized here based primarily on results obtained in-flight during the Servicing Mission Orbital Verification (SMOV) program.

2. Corrector Alignment and Performance

Alignment of STIS consisted of essentially two steps. First, during ground calibration, all optics and detectors were adjusted to properly re-image the STIS slit plane onto each detector. This insured that the nominal spectral resolution could be achieved by selection of the appropriate slit. Secondly, the corrector system was aligned in flight to correct and re-image light from the OTA onto the slit plane, producing the greatest concentration of light at this plane and so maximize the instrument throughput and the spatial resolution along the slit.

STIS incorporates a two mirror corrector system. The first mirror, CM1, is a concave sphere mounted on a mechanism which permits in-flight adjustment in focus and tip/tilt. CM1 produces a nearly collimated beam from the OTA and redirects it toward the second corrector mirror, CM2. CM2 is an anamorphic asphere located at a pupil position which redirects and focuses the beam from CM1 onto the STIS slit plane. Adjustment of CM1 in focus provides a focused image at the STIS slit plane and in tip/tilt provides optimal correction of the image by properly positioning the beam onto CM2.

Ground testing using HST simulators had confirmed the capability of the STIS corrector system. In-flight measurements using on-board calibration lamps confirmed that the spectroscopic modes remained focused to the slit plane following launch. Corrector alignment was accomplished through a series of focus and tip/tilt sweeps, initially in the visible, and finally in the ultraviolet, with the ultimate goal being to maximize the ultraviolet transmission through the $0\farcs1 \times 0\farcs09$ aperture. Spectra obtained in the low resolution modes, G140L and G230L, confirm that following the final setting, slit transmission values measured are very close to expectations, namely 39% (121.6 nm), 50% (160 nm), 55% (200 nm) and 60% (270 nm).

Some additional measurements of slit transmission through a few slits have been completed with the CCD and typically show slightly greater transmission (5-15%) than expected. A similar series of measurements with the MAMA detectors in the ultraviolet will be undertaken shortly.

3. Spectral Resolution

Spectral resolution has been measured in all the STIS primary science modes. For scanning modes, in-flight measurements have typically been made at only a few settings so far, with the remainder to be made shortly. These measurements are made using the single on-board Pt-Cr/Ne calibration lamp (LINE) which illuminates the entire slit plane at a focal ratio similar to the OTA. The selected slits for all measurements are those nominal slits which project to about 2 pixels width at the respective detectors. Uniform slit illumination will yield values which are slit limited. Higher resolution may be achievable, even through these

slits, with point sources which are well focused at the slit plane and so underfill the selected slit. Gaussian fits were made to the line profiles and the fwhm values of these fits have been used to specify the resolving power. No significant differences have been measured between these in-flight tests and similarly produced ground tests which confirmed that STIS achieves, and generally surpasses its spectral resolution requirements. The results are presented as resolving power for first order prime modes in Table 1, echelle modes in Table 2 and first order support modes in Table 3. Values in italics are from ground testing.

3.1. First order, long slit modes

The $52'' \times 0\farcs050$ slit, SL050, was selected for UV measurements (115-310 nm) with the MAMA detectors and the $52'' \times 0\farcs10$ slit , SL100, for CCD measurements (>310nm). The results are shown in Table 1 with ground measurements indicated in italics. The resolving powers indicated include variation over the bandpass and the field for each mode. For the scanning modes, the projection of the slit width at the detector plane is reduced due to the grating anamorphic magnification to about 1.5 pixels for G140M and G230M and about 1.7 pixels for G430M and G750M.

The resolution along the slit length varies ≤10% in bands 2,3 and 4 (165-1000nm). The far-UV modes (G140L, G140M) show more variation: ≤10% over ∼75% of the slit length for G140L, degrading to 70% of the field center value at one end of the slit, and 30% variation over the central half slit length for G140M. Both modes however, meet their pre-flight resolution specifications over >70-75% slit length.

Table 1. Spectral Resolving Power, First Order Primary Modes

Mode	Specification	Measured	Name/λ	Slit
G140L	770-1130	1210-947 (130nm)	P1/143nm	SL050
	(115-170nm)	1440-1039 (155nm)		
G140M	0.86-1.28x10^4	*12070-7760 (117nm)*	P1/117nm	SL050
	(115-170nm)	14370-9240 (137nm)	P5/137nm	SL050
		19340-12380 (164nm)	I6/164nm	SL050
G230L	415-730	670-502 (190nm)	P1/238nm	SL050
	(165-310nm)	950-775 (269nm)		
G230M	0.75-1.39x10^4	*9800-8180 (169nm)*	P1/169nm	SL050
	(165-310nm)	15810-14440 (234nm)	P9/238nm	SL050
		20640-17550 (306nm)	P18/306nm	SL050
G430L	445-770	540-990	P1/430nm	SL100
	(305-555nm)			
G430M	4.34-7.73x10^3	*6200-4940 (317nm)*	P1/317nm	SL100
	(305-555nm)	8002-6460 (445nm)	P6/445nm	SL100
		10140-8390 (522nm)	P9/522nm	SL100
G750L	425-680	650-560 (610nm)	P1/775nm	SL100
	(550-1000nm)	760-690 (820nm)		
G750M	3.76-6.22x10^3	*5490-5150 (573nm)*	P1/573nm	SL100
	(550-1000nm)	8420-6490 (780nm)	P5/780nm	SL100
		10370-8890 (1036nm)	I1/1036nm	SL100

[†]Results in italics are based on ground testing

3.2. Echelle modes

Spectral resolution measurements were made with the 0.″60 wide (S200X060) and 0.″90 wide (S100X090, S200X090) slits for the medium and high dispersion echelle modes respectively. The results are presented in Table 2. The medium resolution echelles exceed their specified resolutions as shown. The E140M echelle used in-flight was a late replacement to the nominal grating which suffered from low efficiency. Used at about 45° instead of the original design 32°, this grating has higher resolution, as indicated, than the companion E230M grating.

The spectral resolving powers of the high resolution echelle modes, E140H and E230H, in Table 2 were measured using the on-board calibration line lamp. While comparable results have been obtained during ground and flight testing, thus confirming the stability of alignment, these modes are capable of much higher resolution. Ground measurements using a mono-isotopic Pt lamp (the on-board lamps are poly-isotopic) with the narrow 0.″025 wide slit (S100X025) gave resolving powers of 132,000-170,000 for the E230H mode. To obtain these results, flat field correction was applied to the spectra in the unbinned, high resolution MAMA formats. Even higher resolution (220,000) was obtained in mode E140H by the same methods and additionally, by removing the voltage which establishes a repelling field in the FUV MAMA. This reduces the detector contribution to PSF by more tightly confining emitted photoelectrons.

Table 2. Spectral Resolving Power, Echelle Modes

Mode	Specification	Measured	Name/λ	Slit
E140M	24,000-24,200 [a] (115-170nm)	46,000	P1/143nm	S200X060
E140H	100,000 (115-170nm)	99,300-114,200 [b]	P2/142nm	S200X090
E230M	23,900-23,100 (165-310nm)	31,000-32,000	I5/256nm	S200X060
E230H	100,000 (165-310nm)	106,000-116,000 [b] *92,300-100,700*[b]	P4/251nm P6/301nm	S100X090 S200X090

[†]Results in italics are based on ground testing

[a]Resolving power specification is for the original, design grating. For the as-flown echelle, the equivalent specification resolving power is 37,000.

[b]Resolving powers are as measured with the on-board poly-isotopic calibration lamps. Potential mode resolving power is greater - see text.

3.3. Support modes

Ground test measurement results of the spectral resolution of the STIS support modes are shown in Table 3. These modes use the echelle mode, cross disperser gratings in first order to produce intermediate resolution in the ultraviolet. A small set of orthogonal slits have been provided to be used with these support modes.

4. Spectrograph Spatial Resolution

Measurements have been made of the extent of illumination perpendicular to spectral dispersion in the primary science modes. The data used was mostly obtained for sensitivity

Table 3. Spectral Resolving Power, First Order Support Modes

Mode	Specification	Measured	Name/λ	Slit
X140M	768-1123	*880-700 (122nm)*	P1/143nm	S050X31B
	(115-170nm)	*1680-1430 (172nm)*		
X140H	2735-3446	*3535-2500 (123nm)*	P1/123nm	S050X29
	(115-170nm)	*4490-3630 (159nm)*	P3/159nm	S050X29
X230M	838-1504	*1300-1020 (159-204nm)*	P1/198nm	S050X31A
	(165-310nm)			
X230H	2437-4391	*3220-2880 (163-183nm)*	P1/176nm	S050X29
	(165-310nm)	*5400-4420 (239-263nm)*	P4/251nm	S050X31A

†Results in italics are based on ground testing

calibrations with various stellar targets at field center using the $52'' \times 2''$ slit. Figures 1 and 2 show the fraction of total illumination in the cross dispersion profile for different extraction heights. In table 4 are presented the best Gaussian fit fwhm at selected wavelengths and the fraction of light in the cross dispersion profile within 2 and 11 pixel total extraction heights for the primary, long slit modes. Similar results for the echelle modes are presented in Table 5, where however, the fraction of light is presented, normalized to the value in 11 pixels.

Figure 1 shows that there is a clear and consistent improvement in light concentration with increasing wavelength in the ultraviolet modes. This reflects the improved performance of the OTA as well as within STIS at longer wavelengths, with peak performance near 300 nm. Note that the plate scales differ by about 20% between first order low and medium resolution modes shown in Figure 1. If OTA scatter were the only effect present, one would expect equal enclosed energy in 12 pixels of G140L as 10 pixels of G140M. This is seen near 160nm, but not near 118nm where the low order mode has better performance. Table 4 also shows slight but consistently smaller fwhm for spatial profiles in low compared to medium resolution modes in the ultraviolet. As the medium resolution modes have two additional mirrors within STIS compared to the low resolution modes, this difference may be due to the additional accumulation of wavefront error in STIS most apparent at the shortest wavelengths. However, measurements of the spatial fwhm from repeated observations in modes G140L and G230L show occasional differences as great as 20% presumably due to a combination of OTA "breathing" and possible drift. Interpretation of the cause of differences smaller than this are thus highly uncertain.

Figure 2 shows a similar trend of improved light concentration with wavelength in the CCD modes from 170-300nm with comparable performance to about 550nm. Longward of this however, diffraction, and more significantly, the diffusion of light within the CCD chip ("halo") is evident, lowering the fraction of light within a given extraction height, though as shown in Table 4, the fwhm of the spatial profile is nearly constant (about 2 pixels = $0''.1$) at all CCD wavelengths.

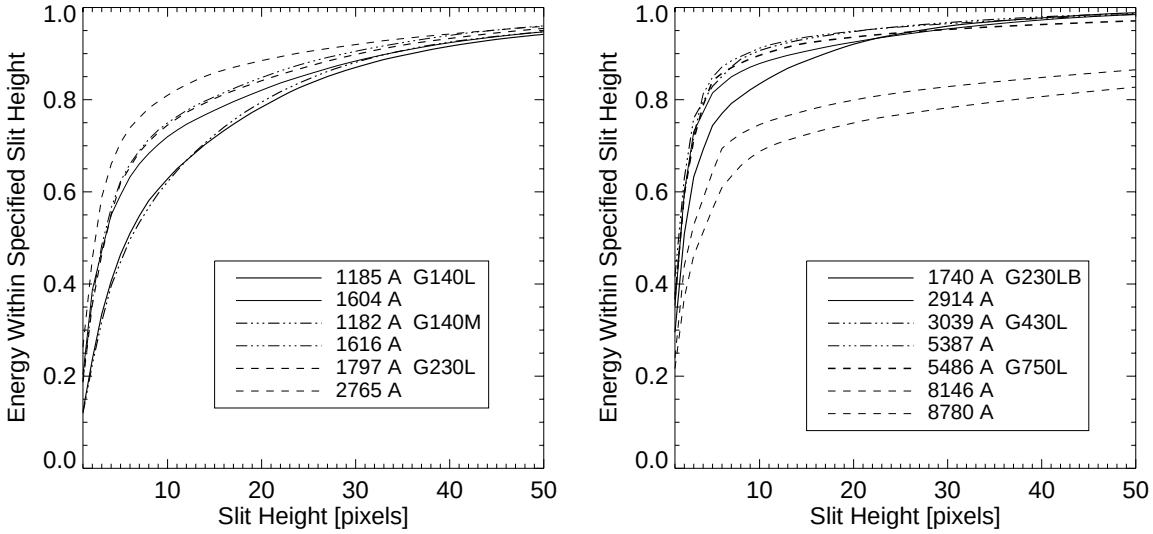

Figures 1 and 2: These figures show the fraction of energy, perpendicular to the dispersion direction, within an indicated extracted, slit height. Results are shown for the MAMA detectors at selected wavelengths in figure 1(left), and for the CCD detector in figure 2(right). Note that the results are expressed in pixels. The MAMA plate scales are about 25mas/pixel and 29mas/pixel for low and medium resolution modes respectively, while the CCD plate scale is about 51mas/pixel.

Table 4. Spatial Resolution - First Order Modes

Mode	FWHM [pixels]	FWHM [arcsecs]	Wavelength [nm]	fld pos	EE 2pix	EE 11 pix	frame
G140L	3.9	0.10	119	ctr	0.24	0.65	1767
	2.4	0.06	160	ctr	0.39	0.73	1767
G140M	4.1	0.12	119	ctr	0.23	0.65	1537
	3.0	0.09	162	ctr	0.37	0.76	1539
G230L	3.2	0.08	180	ctr	0.36	0.76	1742
	2.5	0.06	277	ctr	0.46	0.82	1742
G230M	3.4	0.10	169	ctr	0.31	0.69	1541
	2.6	0.08	298	ctr	0.41	0.74	1547
G430LB	2.1	0.11	174	ctr	0.51	0.85	672
	1.9	0.10	291	ctr	0.60	0.89	672
G430L	1.9	0.10	304	ctr	0.63	0.91	1345
	1.9	0.10	539	ctr	0.59	0.92	1345
G430M	2.0	0.10	309	ctr	0.55	0.89	1358
	1.8	0.09	538	ctr	0.62	0.92	1368
G750L	1.9	0.10	549	ctr	0.60	0.90	676
	2.2	0.11	878	ctr	0.37	0.70	676
G750M	2.1	0.11	754	ctr			1373
	2.0	0.10	10208	ctr			1376

Table 5. Spatial Resolution - Echelle Modes

Mode	FWHM [pixels]	FWHM [arcsecs]	Wavelength [nm]	fld pos	EE 2pix/11pix	EE 11 pix	frame
E140M	2.8-3.3	0.08-0.10	119	ctr	0.47	1.00	4420
	2.2-2.5	0.07	156	ctr	0.60	1.00	4420
E140H	2.6-3.0	0.08-0.09	130	ctr	0.53	1.00	4489
E230M	1.8-2.1	0.05-0.06	287	ctr	0.65	1.00	4416
E230H	2.8-2.9	0.08-0.09	271	ctr	0.53	1.00	3550

5. Sensitivity

A companion paper by N. Collins and R. Bohlin (Collins and Bohlin 1997) presents the results of the initial sensitivity calibrations. Here we will concentrate on those areas where there are significant differences from the early estimates as detailed in the STIS Instrument Handbook or pre-launch testing. In general, sensitivities determined on-orbit are within 20-30% of the estimates presented in the Instrument Handbook and based on component build up estimates. Differences are generally due to slightly different grating blaze angles than exact design specifications. Such a difference leads to less sensitivity at one end of the bandpass and greater sensitivity at the other end. At wavelengths where the sensitivity changes rapidly (typically shortward of the grating blaze peak) a small blaze shift can result in a significant sensitivity change. In most cases the greatest difference occurs where the absolute sensitivity was very low already. An example is in mode G230M where the measured sensitivity is about 60% of the handbook value near 170nm, about the same near 230nm, and about 15% greater near 290nm. G430L sensitivity is sufficiently shifted that the flight value is about 50% greater than the handbook value near 310nm and about nominal from 450nm and longward to 550nm. G430M is more sensitive than handbook values throughout the range: about 60% near 310nm, 35% near 450nm, 25% near 520nm. Both long wavelength CCD modes (G750L, G750M) have lower than anticipated sensitivity at the longest wavelengths due to the CCD halo, G750L about 60% of expected and G750M about 70% near 1000 nm. These sensitivities are defined using nominal extraction heights of 11 pixels for all modes except G430L and G750L for which 7 pixel extractions were used. Preliminary comparisons of echelle sensitivities (typically using wider slits than would be used for normal observations) indicate as expected or higher sensitivity throughout their bandpass for the slits used. The high UV transmission measured at the slit suggests that these modes will be as sensitive or greater than anticipated.

Modes, G140L, G230L and G230LB, show about 25% less sensitivity in-flight than ground testing indicated, through the region 140-220 nm. This is a region in which many typical contaminants show significant thin film absorption. Repeated measurements during ground testing showed no change in the UV efficiency of STIS during testing. Continued monitoring of G140L indicates that the sensitivity between 150-170nm may have declined about 2% over 14 weeks, with no change from 128-140nm. No change throughout the bandpass of G230L can be detected in the same time. Ongoing contamination monitoring will allow more firm limits to be placed on any sensitivity instability.

6. Camera Performance

Camera modes are provided for each STIS detector, primarily for target acquisition but also for scientific purposes. A small complement of filters are provided as well as clear, full field apertures. (Filter characteristics, including red leak data, may be found in the STIS Instrument Handbook with updates.) The open aperture modes of the CCD and FUV cameras as well as the NUV camera with the SrF_2 or crystal quartz filters, have very broad

bandpasses defined by the detector and system optical response. They have significantly greater grasp than other existing HST instruments. The nominal CCD field of view is $50'' \times 50''$ (open aperture) or $25'' \times 50''$ (filtered), and the MAMA detectors have $25'' \times 25''$ fields.

A limited series of in-flight tests have been performed to assess camera performance. The results are summarized in Table 6. In some cases, initial measurements have been obtained only at field center as indicated. As a performance criterion, the encircled energy in a $0\farcs1$ diameter circle is listed (column 5). A reference value (column 6) is the OTA only encircled energy in a $0\farcs1$ diameter circle based on interpolations of the information in Figures 11.13 and 11.14 of Schroeder (1987). The STIS detectors alone will reduce these OTA values as will any residual wavefront error, however these reference values provide a useful benchmark of the maximum possible performance with a well corrected OTA. Typically, 70-85% of the corrected OTA light within $0\farcs1$ diameter will be contained within the same diameter in the STIS images.

Table 6. STIS Camera Performance Summary

Mode	Filter	Wavelength [nm]	Target	EE(<0.1")	Reference EE(<0.1")
MIRCUV	A25	clear	NGC6681	0.32-0.36 over the full field	
MIRFUV	F25LYA	122	BPM16274	0.27 at field center	0.39 (122nm)
	F25SRF2	>130	NGC6681	0.33-0.39 over the full field	0.45 (145nm)
	F25QTZ	>146	NGC6681	0.39-0.43 over the full field	0.49 (155nm)
MIRNUV	F25CN182	182	NGC6681	0.40-0.48 over 2/3, 0.30-0.40 over 1/3	0.56
	F25C3	191	LS749B	0.41 at a single, off-center field point	0.58
	F25CN270	270	NGC6681	0.50-0.54 over 2/3 field 0.40-0.50 over 1/3 field	0.63
	F25MG2	280	BPM16274	0.51 at field center	0.63
	F25SRF2	>130	-	data not yet acquired	
	F25QTZ	>146	-	data not yet acquired	
MIRVIS	A50	clear	Omega Cen	0.47 in 2x2 near field ctr 0.38 < 0.1"	-
	F28X50O2	373	Feige 34	0.50 in 2x2 near field ctr 0.41 < 0.1"	0.60
	F28X50O3	501	Feige 34	0.47 in 2x2 near field ctr 0.36 < 0.1"	0.58
	F28X50LP	548	Omega Cen	0.42 in 2x2 near field ctr 0.34 < 0.1"	0.51 (775nm)

The image quality of the camera modes is illustrated in figures 3-5. Each figure is a set of log-stretched and magnified images from single exposures of the clusters NGC6681 (figures 3 and 5) and Omega Cen (figure 4). The relative positions of the stars are indicated in pixel coordinates below each star. The best fit Gaussian fwhm for profiles extracted horizontally and vertically from each star are shown above and to the left of each star. Figures 3 and 4 also show the horizontally extracted profiles, plotted to the right of the corresponding images.

Figure 3 is of the cluster NGC6681 obtained in a single exposure (1100 seconds) using the far ultraviolet camera without any filter (MIRCUV,A25). Each pixel is about 25mas and the total field around each star shown is $1\farcs27 \times 1\farcs27$. The horizontal branch stars have temperatures of typically 8000-15000 K; the flux weighted camera response will be toward the lower end of the camera range, near 120 nm. The halo seen around each star is due to a combination of OTA scatter, STIS internal scatter and wavefront error, and detector PSF, all of which increase at shorter wavelengths. In the log-stretched images, this halo is seen to be asymetric. The profiles show more accurately the relative amount of light in the halo.

Figure 4 shows stellar images in the field of Omega Cen obtained in a single, 64 second, unfiltered exposure using the CCD (MIRVIS,A50). Each pixel in this image is about 51mas, about twice that of the MAMA camera modes. Some small residual asymmetry of the PSF

is still evident in the corners of the field but the image quality is generally good with fwhm of about two pixels or 102mas.

Figure 5 illustrates the effects of OTA "breathing" (secondary mirror motion due to orbital thermal variations) on the STIS ultraviolet camera modes. The image sets shown are from two exposures, 500 seconds long and separated by 2080 seconds. These were extracted from a single time-tagged 2600 second exposure. The target was again the cluster NGC6681 and the camera was the NUV MAMA with the 270nm, continuum filter (MIRNUV,F25CN270). In the first image set, the image quality degrades on the left side of the detector, but is relatively good (about 2.2 pixels fwhm) over the center and right side. In the second image set, this pattern has switched, with the left side of the field now in good focus and the right side clearly defocused. In both cases, the central, vertical strip stays in relatively good focus. The complement of spectroscopic and camera modes for each MAMA may direct light onto each detector from any of four different directions. The detectors were oriented to optimize the performance in the spectroscopic modes. This results in a tilt between the MAMA camera mode focal planes and the detector plane, creating a cylindrical symmetry to the camera mode field imagery. Movement of the OTA secondary ("breathing") results in a relative defocus of the camera focal planes with respect to the MAMA detectors, the line of best focus sweeping across the detector. With the center of the field at nominal focus, little effect is seen as long as the defocus is less than the depth of focus. However the edges of the camera fields are nominally near the limits of the focal depth so that any further defocus creates a noticeable degradation on one side of the field and improvement on the opposite side. The results seen with STIS are consistent with the typical OTA breathing, secondary displacements of several microns. Values for encircled energy in Table 6 are thus time averages.

The flux transmitted through a spectrographic slit at the field center is relatively insensitive to OTA breathing. Modelling of the PSF at the slit plane at 125nm for a 60mas wide slit shows about 10% lower transmission for a $1''$ long slit and about 20% loss for a very short, $0\farcs1$ slit, for a characteristic maximum secondary excursion of 5 microns. Examination of two time tag spectroscopic observations using the $0\farcs2 \times 0\farcs09$ slit shows a variation of no more than 10% transmitted flux over 2000 seconds, which loss includes any drift as well as breathing effects.

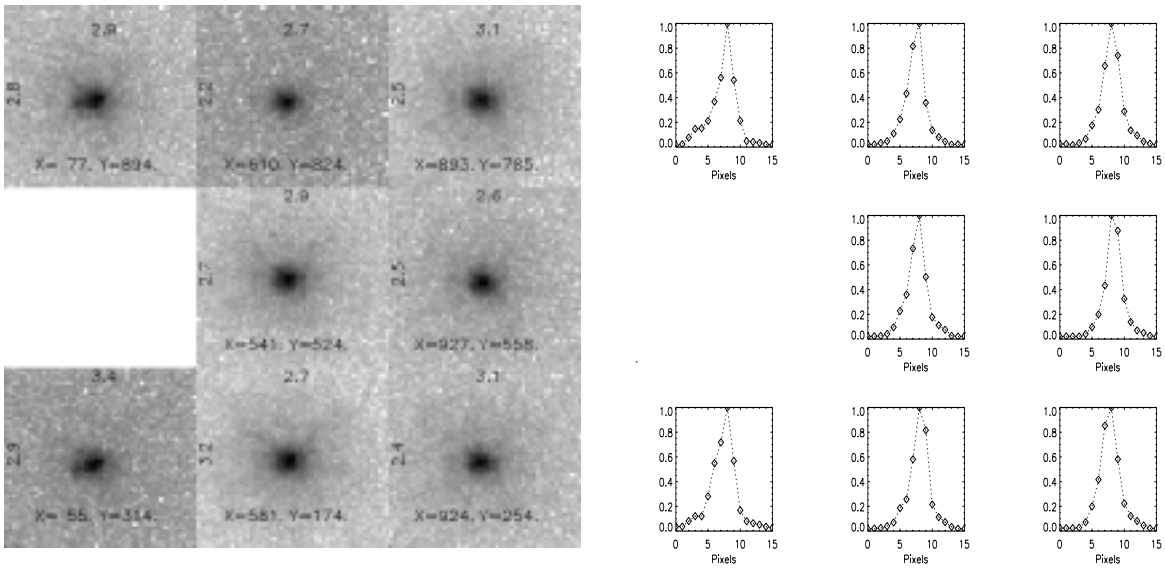

Figure 3: Figure 3a (left) is a log-stretched set of stellar images from an 1100 second exposure of NGC6681 taken with the far-UV MAMA without a filter. Each pixel is about 25mas with a total field around each star of about $1\farcs3 \times 1\farcs3$ (51 pixels). The Gaussian fit fwhm to vertical and horizontal extracted profiles are given in pixels, to the left and above each star. The flux weighted camera response peaks <130 nm, where STIS residual wavefront error and OTA scatter are greatest. These result in the asymmetric images seen near the corners of the field and the halo around each star. Figure 3b (right) shows horizontally extracted profiles of each star in the field indicating the relative flux distribution.

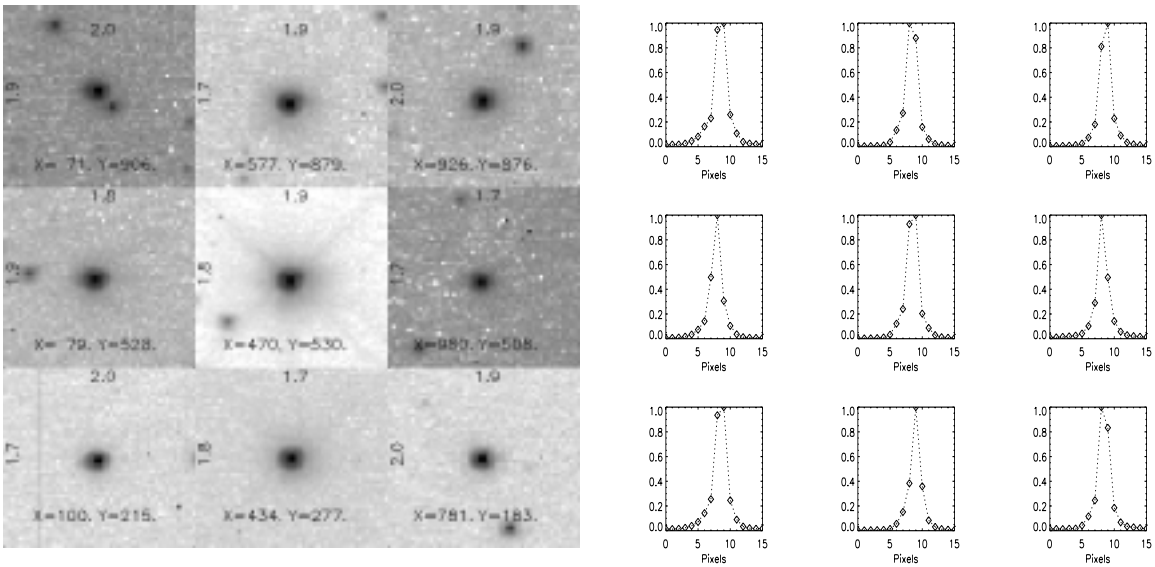

Figure 4: Figure 4a (left) shows a similar set of stellar images from a 64 second exposure of Omega Cen acquired with the unfiltered, CCD camera. The plate scale is about twice that of the ultraviolet images, 51mas/pixel with $2\farcs6 \times 2\farcs6$ field around each star. Corresponding horizontal, extracted profiles are shown in the adjacent figure 4b (right). Image quality is generally uniform across the field, with small asymmetries of the PSF most evident in the field corners.

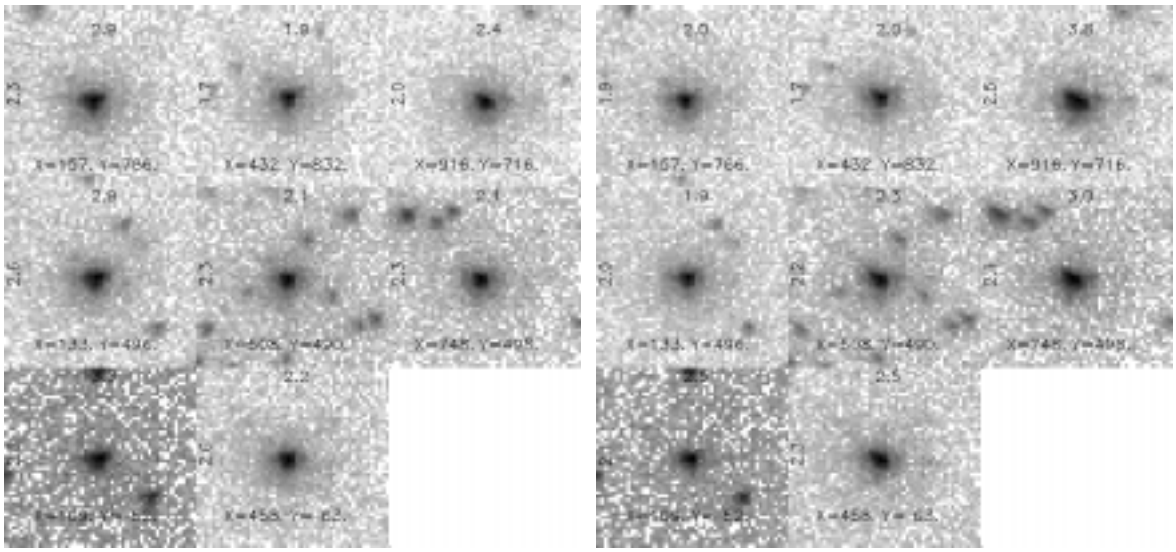

Figure 5: The effects of OTA breathing on STIS imagery are illustrated in these two log-stretched images of stars in the field of NGC6681 acquired with the NUV MAMA using the CN270 filter. The same stars are shown in both image sets, labeled by their X,Y locations in pixels. The best fit Gaussian fwhm to the extracted vertical and horizontal profiles are indicated to the left and above each image (fwhm values in pixels where 1pix = 25mas). Each exposure was 520 seconds long with 2080 seconds separating the two exposures. The first exposure (left) shows degraded performance to the left of center, due to defocus at the detector plane. By the time of the second exposure (right), the OTA secondary had shifted in position causing a corresponding shift in the camera focal plane. Stars on the left side of the field are now in good focus while stars on the right side of the field are now defocused. Images of stars along the vertical, central strip are less sensitive to breathing: the focal shift was approximately within the depth of focus of these images.

Acknowledgments. We would like to thank all those whose hard work and perseverance through the years have resulted in the successful construction, testing, installation and commissioning of STIS. The STIS IDT has been funded in response to NASA Announcement of Opportunity OSSA-4-84 through the *Hubble Space Telescope Project* at the Goddard Space Flight Center. This paper is based on observations with the NASA/ESA *Hubble Space Telescope*, obtained at the Space Telescope Science Institute, which is operated by the Association of Universities for Research in Astronomy, Inc. (AURA), under NASA contract NAS5-26555

References

Baum, S. et al. 1996, *STIS Instrument Handbook*, STScI: Baltimore

Collins, N. & Bohlin, R. 1997, this volume

Content, D. A. et al. 1997, Proc. SPIE, 2807, 267

Schroeder, D., 1987 in *Astronomical Optics*, San Diego: Academic Press, 216

Woodgate, B. et al. 1992, ESO Conf. and Workshop Proc. 44: Science with the Space Telescope, P. Benvenuti & E. Schreier, European Southern Observatory: Munich, 525

Woodgate, B. et al. 1998, in preparation